

Single-pixel-based Hyperspectral Microscopy

Lisa Uguen,¹ Ronan Piedevache,¹ Gaspard Russias,¹ Sofian Helmer,¹ Denis Tregcoat,¹ and Stephane Perrin¹
Biophotonics Group, Photonics Bretagne, 4 Rue Louis de Broglie, 22300 Lannion, France

(*Electronic mail: sperrin@photonics-bretagne.com)

(Dated: 12 July 2024)

Hyperspectral imaging allows to collect both spatial and quasi-continuous spectral information of an object. This work shows the innovative combination of single-pixel microscopy with hyperspectral imaging. An affordable hyperspectral microscope is able to observe micrometer-scale features of inorganic and biological samples and to reconstruct their spectral distribution with a high accuracy (*i.e.* a spatial and a spectral resolution of 9.0 μm and of 2.1 nm in the visible range, respectively). Furthermore, a statistical algorithm enables the identification of spectral responses of the targeted features as well as their classification.

Hyperspectral imaging enables the collection of the spectral distribution of an object (*i.e.* an hypercube) encoded over hundreds of bands, unlike multispectral imaging where the spectrum is only divided in a few bands. Hyperspectral imaging systems are usually based on a spatial encoding method where the optical head is scanned above the sample using a punctual approach (*i.e.* *whiskbroom* imager)^{1,2} or a linear approach (*i.e.* *pushbroom* imager)³. The hypercube may also be spectrally encoded, for example, using a wavelength-tunable illumination source⁴ or an array of Fabry-Pérot filters⁵. Fourier-transform infrared spectroscopy⁶, where the spectral properties are extracted from an interference signal using Wiener-Khinchin theorem, has been investigated in the visible⁷ and in the mid-infrared ranges⁸. These works have led to significant benefits, for example in life sciences for identifying plant diseases^{9,10}, analysing biochemical processes¹¹, and classifying tumour cells¹². Despite recent hardware advances where accessible hyperspectral imaging is promoted¹³⁻¹⁵, this imaging technique is still not used much in industry⁵, and even less in microscopy¹⁶. Indeed, it may appear expensive or complex to implement¹⁷. The spectral resolution (or the number of spectral bands) and the frame rate may also hinder some applications.

Recent advances using single-pixel detection have been reported in hyperspectral imaging working in the visible^{18,19} and near-infrared regions²⁰. In single-pixel imaging, the averaged intensity of a scene onto which a sequence of illumination patterns is superimposed, is usually recorded²¹. Acquisitions using a passive mode may also be considered by modulating the incident intensity on the detector²². The spatial intensity distribution of the scene is then retrieved by operating an inverse transform on the mask basis. Several orthogonal bases subsist (*e.g.* using Fourier, Hadamard, discrete-cosine, or wavelet transform). The performance of convolutional neural networks has also been exploited to reconstruct the scene with a high signal-to-noise ratio²³. Furthermore, in order to deal with the negative-value issue, phase-shifting²⁴ and splitting-component²⁵ methods have been investigated. The spatial resolution of classical single-pixel imagers is however limited by the ability of the illumination system to project high-spatial-frequency patterns and thus the acquisition time. Indeed, the higher the lateral resolution, the lower the frame rate is.

Enhancement of the lateral resolution in single-pixel imag-

ing has thus been suggested by introducing a microscope objective²⁶ ($\sim 3 \mu\text{m}$ resolution with 128×128 pixels). Moreover, variants have been developed where a digital micromirror device (DMD) is used to continuously scan the sample²⁷. A transmission-mode single-pixel microscope has allowed to observe transparent cells using a liquid crystal spatial light modulator in the illumination path²⁸. These works have led to original studies in hyperspectral microscopy highlighting low-absorption samples²⁹ or working in the mid-infrared region³⁰. Furthermore, Klein *et al.* have developed a transmission-mode hyperspectral microscope where the collected frame is spatially encoded³¹. A spatial resolution down to 7 μm is achieved in the visible range.

In this work, a single-pixel hyperspectral microscope working in the visible and near infrared ranges was developed in reflection mode. The hyperspectral microscope consists of a structured illumination method, where successive patterns are projected on the sample using a DMD-based projector. The hypercubes of the samples are reconstructed using a Hadamard-basis algorithm. This affordable imaging technique allows to retrieve the spectral reflectance distribution of non-organic and biological samples at the micrometer scale with a high accuracy. Moreover, a segmentation algorithm was implemented to identify the spectral response of microorganisms and micro-structures.

Figure 1 shows the experimental setup of the reflection single-pixel hyperspectral microscope. The illumination system of the microscope is set up on a Köhler architecture where the light comes from a DMD-assisted projector (P). The generated Hadamard patterns are collected by two lenses (L1 and L2) which image the 800×600 -pixels-size binary frames in the field diaphragm plane. Hadamard basis allows not only to avoid the generation of Moiré patterns which leads to low-frequency noises, but also to reconstruct high-quality hypercubes³². The structured illumination beam is then directed through the microscope objective (MO) by a beam splitter cube (BSC1). The two lenses are used both to adapt the beam diameter with the entrance pupil of the microscope objective ($\times 20$, NA = 0.4) and to maximise the high-spatial-frequency projection in the object plane. Note that the focal length ratio of the two lenses and the magnification factor of the objective limit the spatial frequency of the Hadamard patterns. In addition, an optical density window introduced in the

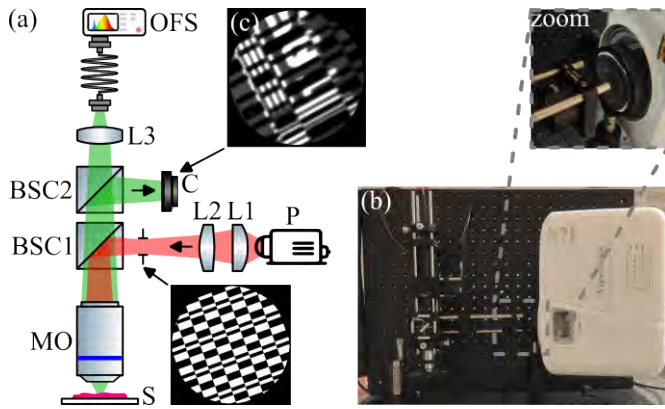


FIG. 1. Single-pixel hyperspectral microscope. (a) Layout of the imaging system. P, projector. L, lens. BSC1 and BSC2, beam splitter cubes. MO, microscope objective. S, sample. OFS, optical-fiber spectrometer. C, camera. (b) Photograph of the on-bench imaging system with a zoom view on the lenses L1 and L2. (c) Camera view of a Hadamard pattern superimposed on a resolution target.

field diaphragm plane optimises the illumination irradiance and avoid the light to damage biological samples (*e.g.* burn mark). In the object plane, the contrast of the Hadamard patterns reaches up to 65%. The back-scattered signal from the sample superimposed with a Hadamard pattern is then propagated by the microscope objective through a second R10:T90 beam splitter cube (BSC2). The reflected frame is imaged on a camera (C) in order to observe in real-time the object field (Fig. 1(c)). Finally, the transmitted irradiance is focused by a lens (L) to enhance the injection ability into an optical fiber with a core diameter of 400 μm . At the end of the optical fiber, a spectrometer samples the averaged spectral intensity of 25 acquisitions per binary-pattern projection. Due to the high-optical-power of the projector, the exposure time of the spectrometer is down to 7 ms depending on the sample to observe. The synchronisation of the spectrometer with the projector is made with a software trigger as described in Ref.³³. The most expensive element of the hyperspectral microscope is the spectrometer for 4,000 €. The cost of the imaging system, taking into account all the other necessary elements (*i.e.* the video-projector, the objective lens and the optical components), reaches around 5,000 €.

First, positive resolution targets were introduced in the object plane of the objective lens (Fig. 2(a)) to determine the spatial performance of the single-pixel hyperspectral microscope. The pixel size in the object plane (*i.e.* spatial sampling) is 3.8 μm . With 51×51 pixels, the resolution power of the microscope reaches 9 μm , almost twice the Nyquist rate. This resolution power is similar to the one in Ref.³¹. The normalised reflectance of the 6- μm -wide lines along two transverse directions shows a mean reflectance contrast around 70% (Fig. 2(b)). The frame in Fig. 2(a) was reconstructed using the red, green and blue bands from the raw spectrum of the hypercube. Figure 2(c) shows the reflectance intensity distribution of a Lambertian diffuse standard (Spectralon®, LabSphere) having a constant reflectance

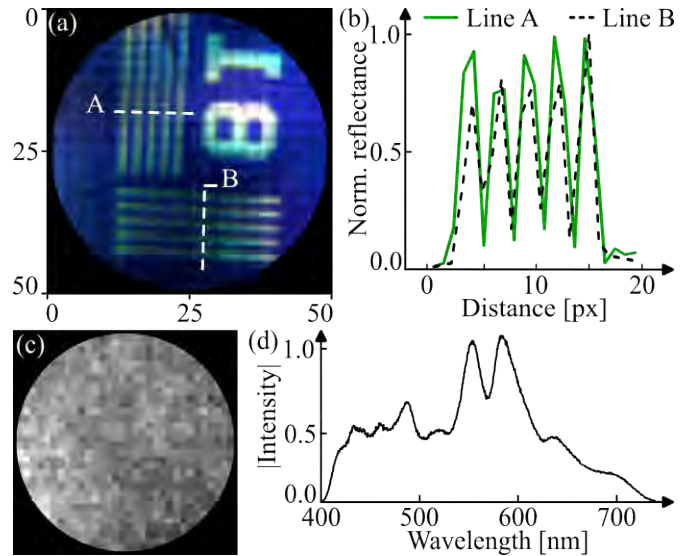


FIG. 2. Spatial and spectral performance of the single-pixel hyperspectral microscope. (a) RGB-image reconstruction of a 81-lines/mm-frequency resolution target. (b) Normalised reflectance from the A and B white-dashed lines as a function of the lateral distance. (c) Reflectance distribution of a calibrated standard. (d) Normalised spectral intensity of the illumination source averaged over the standard surface.

factor of 50% over the visible and the infrared ranges. With a calibrated diffuse response, it enables to define the standard deviation of the spectral distribution ($\sigma = 9\%$) over the field of view of the microscope. Also, it is used to quantify the reflectance distribution of the samples from their measured hypercube. For this, the raw spectra per pixel are normalised with the spectral intensity of the standard (Fig. 2(d)). Note that the spectrometer consists of a 2048-pixel line sensor working between 300 nm and 1100 nm. In our case however, the projector lamp limits the spectral range of the hyperspectral microscope to around 750 nm (Fig. 2(c)). The spectral resolution was separately characterised using a Ar/Hg light source: a 2.1 nm value was obtained.

Algae are aquatic plant-like organisms having a C_3 carbon fixation metabolic pathway³⁴ in which the nitrogen concentration is proportional to the chlorophyll content³⁵. Nitrogen thus influences the spectral response, especially in the green region (and at around 750 nm). This optical effect was used to discriminate spectrally two micro-powders of freeze-dried *Ulva lactuca* algae with nitrogen concentrations of 4.02 g and 1.04 g per 100g of dry matter. These values were previously quantified by analytical methods in a certified laboratory. The dark-green algae powder was harvested in spring and the light-green powder, in summer. The two powders were placed next to each other on a glass slide using a reflective-mode light microscope (Leica ICC50W, Fig. 3(a)). The hypercube of the samples was then recorded through the hyperspectral microscope from which the RGB-basis image is reconstructed (Fig. 3(b)). The spectral distribution enables to spatially segment the algae powders (Clusters #1 and #2), the

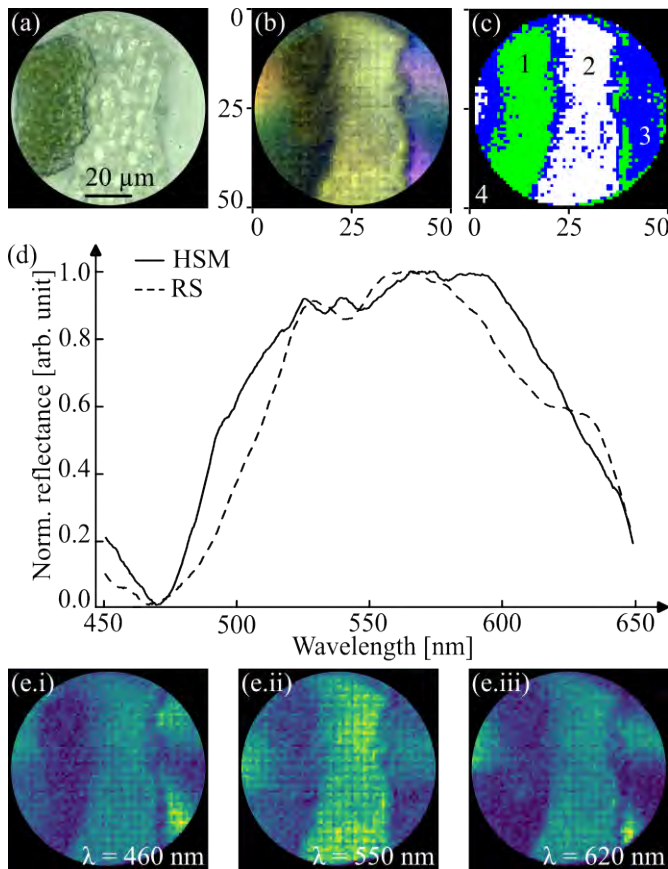


FIG. 3. Micro-powders of *Ulva lactuca* algae through hyperspectral microscopy. (a) Observation of algae having nitrogen concentrations of 4.02 g (dark green) and 1.04 g/100g (light green) under the microscope ($\times 20$, $NA = 0.4$). (b) RGB-reconstructed image from the hypercube of the sample (52×52 px). (c) Segmentation of the sample using 4 optimal clusters. (d) Averaged spectral reflectance of the dark-green alga (Cluster #1) compared with reflectance spectroscopy (RS). (e) Intensity frames from the hypercube at three wavelengths.

glass substrate (Cluster #3), and the field-diaphragm surface (Cluster #4) by implementing a principal component analysis (PCA) followed by a K-means clustering (Fig. 3(c)). Note that the substrate area appears in blue in Fig. 3(b) due to the longitudinal chromatic aberration of the microscope objective (*i.e.* out of object plane). Artefacts in the segmentation appear from the fact that some features of the samples are not clearly resolved but are just distinguished by the imaging system (*e.g.* the blue dots in the middle of Cluster #2 which result from the cell membranes). These leads to localized spectral responses which are then considered by the segmentation algorithm. Finally, the spectra of each cluster were averaged and compared to the measurements of classical punctual reflectance spectroscopy. Figure 3(d) shows the normalized spectral responses of the dark-green alga particle using reflectance spectroscopy and hyperspectral microscopy, highlighting a high accuracy ($RMSE = 0.09$). For the light-green particle, the $RMSE$ reaches 0.18. Figure 3(e.i), (e.ii), and (e.iii) show three intensity frames from the hypercube at a wavelength of 460 nm, 550 nm, and 620 nm, respectively.

The *Côte de granite rose* is one of the three places in the world where typical pink granite can be admired. Constituted mainly of quartz and feldspar with haematite impurities (*e.g.* iron(III) oxide), the granite appears to be pink at the macroscopic scale. At a finer scale, the mineral phases of the igneous rock may be observed and distinguished with hyperspectral microscopy. Figure 4(a) shows the direct view of the granite sample (Leica ICC50W). Then, it was placed below the hyperspectral microscope to reconstruct the hypercube (Fig. 4(b)) with a finer spatial resolution than performance reported in scientific literature to date³⁶. The hypercube enables to segment three areas over the field of view (Fig. 4(c)). The spectral reflectance of each cluster was then averaged, highlighting the typical reflectance increase from the ferric iron concentration at a wavelength of 550 nm. The amount of haematite may also lead to a wavelength shift up to 600 nm³⁷. The amplitude difference between the reflectance signals may be explained by the accumulation of haematite during the metamorphic process.

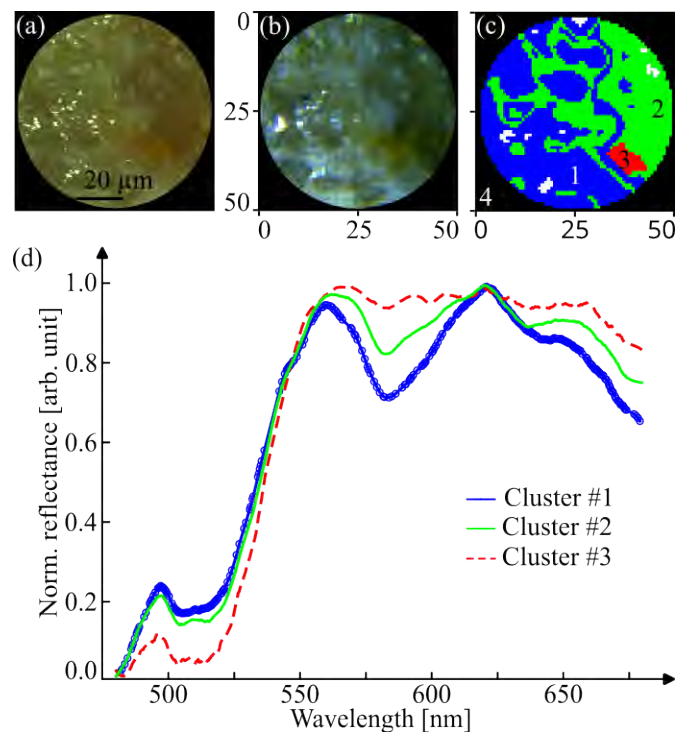


FIG. 4. Mineral phase of pink granite through hyperspectral microscopy. (a) Observation of mineral phases under the microscope ($\times 20$, $NA = 0.4$). (b) RGB-reconstruction image from the hypercube of the sample (52×52 px). (c) Segmentation of the sample using 4 optimal clusters. The white-colour cluster corresponds to saturated areas. (d) Averaged spectral reflectance of the three areas of interest (Clusters #1, #2, and #3).

The spatial resolution of the single-pixel hyperspectral microscope could be enhanced to visualise smaller biological elements (*e.g.* nuclei of cells). For this, the microscope objective should be replaced by one with a higher resolution power, and the spatial frequency of Hadamard patterns could be slightly increased. Indeed, the diffraction from the shape of

the DMD micro-mirrors limits the contrast of high-resolution patterns³¹. Moreover, the acquisition time, currently is around 30 min, could be reduced using, for example, compressive sensing advances where the sampling can be less than defined by Shannon-Nyquist theorem³⁸ or by homogeneous area scanning implemented by Photonics Open Projects where the areas of interest are determined beforehand³³. In these cases, the acquisition time can be seconds.

The analysis of visible-range spectral distribution with a partial least squares regression would allow the prediction of the nitrogen rate at a given position in algae and the identification of microalgae species³⁹. Working in the short-wavelength infrared (SWIR) range offers the possibility to query elements (e.g. sugar and lipid) and to detect sickness at the plant cellular scale. This spectral region could also be interesting in biomedical applications such as for the estimation of hydration and lipid concentrations in skin pathologies⁴⁰. Measuring SWIR-range hypercubes would require a slight enhancement of the single-pixel hyperspectral microscope (e.g. the adaptation of the objective lens). In mineralogy, the infrared-domain spectral signature would allow to identify the various compounds⁴¹.

Finally, a phase retrieval algorithm using the active pattern projection could be implemented to reconstruct the topography in addition to the spectral intensity distribution^{7,42}. This depth information is needed to calculate the bidirectional reflectance distribution function of samples.

A reflective-mode hyperspectral microscope working in the visible range was developed using the principle of active single-pixel imaging. With a spectral resolution of 2.1 nm in the visible range, the microscope is able to encode the continuous spectral signature of small features of biological and inorganic samples with a spatial resolution up to around 9 μm (with 51 \times 51 pixels). The hypercubes of microalgae and of minerals were reconstructed, allowing to distinguish their nitrogen concentrations and to highlight accumulation of haematite, respectively. The overall cost of the imaging system is around 5,000 €. This method provides a significant enhancement in hyperspectral microscopy and future improvements will be considered, such as the spatial resolution and the spectral range.

AUTHOR DECLARATIONS

Conflict of Interest

The authors declare no conflicts of interest. G. Russias and D. Tregoa work part-time with Photonics Open Projects SAS, France.

Fundings

The contributions of S. Perrin was funded by the Research Tax Credit (Ministère de l'Enseignement Supérieur et de la Recherche, France). This work was supported by Région Bretagne, Département Côtes-d'Armor, and Lannion Trégor Communauté.

Acknowledgments

The authors thank Dr. Sophie Richier (Algae Technology and Innovation Centre, France) for providing the algae samples and Dr. Gwenaëlle Lefeuvre for their constructive contribution to the drafting of the manuscript.

Data Availability

The data that support the findings of this study are available within the article.

REFERENCES

- S. Katari, M. Wallack, M. Huebschman, P. Pantano, and H. Garner, "Fabrication and evaluation of a near-infrared hyperspectral imaging system," *Journal of Microscopy* **236**, 11–17 (2009).
- I. V. Novikova, C. R. Smallwood, Y. Gong, D. Hu, L. Hendricks, J. E. Evans, A. Bhattarai, W. P. Hess, and P. Z. El-Khoury, "Multimodal hyperspectral optical microscopy," *Chemical Physics* **498-499**, 25–32 (2017).
- Z. Zhang, B. Hu, Q. Yin, T. Yu, and Z. Zhang, "Optical design and laboratory test of an internal pushbroom hyperspectral microscopy," *Modern Physics Letters B* **33**, 1950143 (2019).
- T. Kääriäinen and T. Dönsberg, "Active hyperspectral imager using a tunable supercontinuum light source based on a mems fabry-perot interferometer," *Optics Letters* **46**, 5533 (2021).
- M. Yako, Y. Yamaoka, T. Kiyohara, C. Hosokawa, A. Noda, K. Tack, N. Spooren, T. Hirasawa, and A. Ishikawa, "Video-rate hyperspectral camera based on a cmos-compatible random array of fabry-pérot filters," *Nature Photonics* **17**, 218–223 (2023).
- P. R. Griffiths and J. A. de Haseth, *Fourier Transform Infrared Spectrometry* (Wiley, 2006).
- S. Marbach, R. Claveau, F. Wang, J. Schiffler, P. Montgomery, and M. Flury, "Wide-field parallel mapping of local spectral and topographic information with white light interference microscopy," *Optics Letters* **46**, 809 (2021).
- D.-C. Soncco, C. Barbanson, M. Nikolova, A. Almansa, and Y. Ferrec, "Fast and accurate multiplicative decomposition for fringe removal in interferometric images," *IEEE Transactions on Computational Imaging* **3**, 187–201 (2017).
- M. Kuska, M. Wahabzada, M. Leucker, H.-W. Dehne, K. Kersting, E.-C. Oerke, U. Steiner, and A.-K. Mahlein, "Hyperspectral phenotyping on the microscopic scale: towards automated characterization of plant-pathogen interactions," *Plant Methods* **11** (2015), 10.1186/s13007-015-0073-7.
- A. Terentev, V. Dolzhenko, A. Fedotov, and D. Eremenko, "Current state of hyperspectral remote sensing for early plant disease detection: A review," *Sensors* **22**, 757 (2022).
- G. Lu and B. Fei, "Medical hyperspectral imaging: a review," *Journal of Biomedical Optics* **19**, 010901 (2014).
- M. Maktabi, Y. Wichmann, H. Köhler, H. Ahle, D. Lorenz, M. Bange, S. Braun, I. Gockel, C. Chalopin, and R. Thieme, "Tumor cell identification and classification in esophageal adenocarcinoma specimens by hyperspectral imaging," *Scientific Reports* **12** (2022), 10.1038/s41598-022-07524-6.
- M. B. Stuart, M. Davies, M. J. Hobbs, T. D. Pering, A. J. S. McGonigle, and J. R. Willmott, "High-resolution hyperspectral imaging using low-cost components: Application within environmental monitoring scenarios," *Sensors* **22**, 4652 (2022).
- E. M. Pechlivani, A. Papadimitriou, S. Pemas, N. Giakoumoglou, and D. Tzovaras, "Low-cost hyperspectral imaging device for portable remote sensing," *Instruments* **7**, 32 (2023).
- A. Al-Hourani, S. Balendhran, S. Walia, and T. Hourani, "Line scan hyperspectral imaging framework for open source low-cost platforms," *Remote Sensing* **15**, 2787 (2023).
- H. Pu, L. Lin, and D. Sun, "Principles of hyperspectral microscope imaging techniques and their applications in food quality and safety detection: A review," *Comprehensive Reviews in Food Science and Food Safety* **18**, 853–866 (2019).

- ¹⁷M. H. Tran and B. Fei, “Compact and ultracompact spectral imagers: technology and applications in biomedical imaging,” *Journal of Biomedical Optics* **28** (2023), 10.1117/1.jbo.28.4.040901.
- ¹⁸M. Ribes, G. Russias, D. Tregoa, and A. Fournier, “Towards low-cost hyperspectral single-pixel imaging for plant phenotyping,” *Sensors* **20**, 1132 (2020).
- ¹⁹Q. Yi, L. Z. Heng, L. Liang, Z. Guangcan, C. F. Siong, and Z. Guangya, “Hadamard transform-based hyperspectral imaging using a single-pixel detector,” *Optics Express* **28**, 16126 (2020).
- ²⁰P. Gattinger, J. Kilgus, I. Zorin, G. Langer, R. Nikzad-Langerodi, C. Rankl, M. Gröschl, and M. Brandstetter, “Broadband near-infrared hyperspectral single pixel imaging for chemical characterization,” *Optics Express* **27**, 12666 (2019).
- ²¹G. M. Gibson, S. D. Johnson, and M. J. Padgett, “Single-pixel imaging 12 years on: a review,” *Optics Express* **28**, 28190 (2020).
- ²²M. P. Edgar, G. M. Gibson, and M. J. Padgett, “Principles and prospects for single-pixel imaging,” *Nature Photonics* **13**, 13–20 (2018).
- ²³G. Beneti Martins, L. Mahieu-Williams, T. Baudier, and N. Ducros, “Open-spyrit: an ecosystem for open single-pixel hyperspectral imaging,” *Optics Express* **31**, 15599 (2023).
- ²⁴L.-T. Meng, P. Jia, H.-H. Shen, M.-J. Sun, D. Yao, H.-Y. Wang, and C.-H. Yan, “Sinusoidal single-pixel imaging based on fourier positive-negative intensity correlation,” *Sensors* **20**, 1674 (2020).
- ²⁵A. Lorente Mur, M. Ochoa, J. Cohen, X. Intes, and N. Ducros, “Handling negative patterns for fast single-pixel lifetime imaging,” in *Molecular-Guided Surgery: Molecules, Devices, and Applications V*, edited by B. W. Pogue and S. Gioux (SPIE, 2019).
- ²⁶N. Radwell, K. J. Mitchell, G. M. Gibson, M. P. Edgar, R. Bowman, and M. J. Padgett, “Single-pixel infrared and visible microscope,” *Optica* **1**, 285 (2014).
- ²⁷X. Dong, G. Tong, X. Song, X. Xiao, and Y. Yu, “DMD-based hyperspectral microscopy with flexible multiline parallel scanning,” *Microsystems & Nanoengineering* **7** (2021), 10.1038/s41378-021-00299-2.
- ²⁸H. Deng, G. Wang, Q. Li, Q. Sun, M. Ma, and X. Zhong, “Transmissive single-pixel microscopic imaging through scattering media,” *Sensors* **21**, 2721 (2021).
- ²⁹K. B. Yushkov, J. Champagne, J.-C. Kastelik, O. Y. Makarov, and V. Y. Molchanov, “AOTF-based hyperspectral imaging phase microscopy,” *Biomedical Optics Express* **11**, 7053 (2020).
- ³⁰A. Ebner, P. Gattinger, I. Zorin, L. Krainer, C. Rankl, and M. Brandstetter, “Diffraction-limited hyperspectral mid-infrared single-pixel microscopy,” *Scientific Reports* **13** (2023), 10.1038/s41598-022-26718-6.
- ³¹L. Klein, J. Touš, and K. Žídek, “Spatially encoded hyperspectral compressive microscope for ultrabroadband vis/nir hyperspectral imaging,” *Applied Optics* **62**, 4030 (2023).
- ³²Z. Zhang, X. Wang, G. Zheng, and J. Zhong, “Hadamard single-pixel imaging versus fourier single-pixel imaging,” *Optics Express* **25**, 19619 (2017).
- ³³Photonics Open Projects, “ONE-PIX,” (2022), <https://github.com/PhotonicsOpenProjects/ONE-PIX>.
- ³⁴N. D. H. Lloyd, D. T. Canvin, and D. A. Culver, “Photosynthesis and photorespiration in algae,” *Plant Physiology* **59**, 936–940 (1977).
- ³⁵J. R. Evans, “Photosynthesis and nitrogen relationships in leaves of c3 plants,” *Oecologia* **78**, 9–19 (1989).
- ³⁶H. L. C. Daempfling, C. Mielke, N. Koellner, M. Lorenz, C. Rogass, U. Altenberger, D. E. Harlov, and M. Knoper, “Automatic element and mineral detection in thin sections using hyperspectral transmittance imaging microscopy (hypertim),” *European Journal of Mineralogy* **34**, 275–284 (2022).
- ³⁷L. C. Canton, I. G. d. Souza Júnior, L. S. Silva, J. Marques Júnior, and A. C. S. d. Costa, “Identification and quantification of iron oxides by diffuse reflectance spectroscopy with praying mantis accessory and integration sphere,” *CATENA* **196**, 104899 (2021).
- ³⁸E. Candes, J. Romberg, and T. Tao, “Robust uncertainty principles: exact signal reconstruction from highly incomplete frequency information,” *IEEE Transactions on Information Theory* **52**, 489–509 (2006).
- ³⁹L. Wei, K. Su, S. Zhu, H. Yin, Z. Li, Z. Chen, and M. Li, “Identification of microalgae by hyperspectral microscopic imaging system,” *Spectroscopy Letters* **50**, 59–63 (2017).
- ⁴⁰Y. Zhao, A. Pilvar, A. Tank, H. Peterson, J. Jiang, J. C. Aster, J. P. Dumas, M. C. Pierce, and D. Roblyer, “Shortwave-infrared meso-patterned imaging enables label-free mapping of tissue water and lipid content,” *Nature Communications* **11** (2020), 10.1038/s41467-020-19128-7.
- ⁴¹C. Pilorget and J.-P. Bibring, “Nir reflectance hyperspectral microscopy for planetary science: Application to the micromega instrument,” *Planetary and Space Science* **76**, 42–52 (2013).
- ⁴²Y. Xu, A. Giljum, and K. F. Kelly, “A hyperspectral projector for simultaneous 3d spatial and hyperspectral imaging via structured illumination,” *Optics Express* **28**, 29740 (2020).